

A spectral study of the black hole X-ray binary MAXI J1820+070 with *AstroSat* and *NuSTAR*

Sudip Chakraborty¹★, Nilam Navale^{2,3}, Ajay Ratheesh^{4,5,6}, Sudip Bhattacharyya¹

¹Department of Astronomy and Astrophysics, Tata Institute of Fundamental Research, Mumbai 400005, India

²University Department of Physics, University of Mumbai, Kalina, Santacruz, Mumbai 400 098, India

³Ramniranjan Jhunjhunwala College, Ghatkopar, Mumbai 400086, India

⁴Department of Physics, University of Rome 'Tor Vergata', via della Ricerca Scientifica 1, 00133, Rome, Italy.

⁵INAF-IAPS, Via del Fosso del Cavaliere 100, I-00133 Rome, Italy

⁶Department of Physics, University of Rome 'La Sapienza', P. le A. Moro 2, 00185 Rome, Italy

Accepted XXX. Received YYY; in original form ZZZ

ABSTRACT

MAXI J1820+070 is a newly discovered transient black hole X-ray binary, which showed several spectral and temporal features. In this work, we analyse the broadband X-ray spectra from all three simultaneously observing X-ray instruments onboard *AstroSat*, as well as contemporaneous X-ray spectra from *NuSTAR*, observed during the hard state of MAXI J1820+070 in March 2018. Implementing a combination of multi-colour disc model, relativistic blurred reflection model RELXILLPCP and a distant reflection in the form of XILLVERCP, we achieve reasonable and consistent fits for *AstroSat* and *NuSTAR* spectra. The best-fit model suggests a low temperature disc ($kT_{\text{in}} \sim 0.3$ keV), iron overabundance ($A_{\text{Fe}} \sim 4 - 5$ solar), a short lamp-post corona height ($h \lesssim 8R_{\text{g}}$), and a high corona temperature ($kT_{\text{e}} \sim 115 - 150$ keV). Addition of a second Comptonisation component leads to a significantly better fit, with the kT_{e} of the second Comptonisation component being $\sim 14 - 18$ keV. Our results from independent observations with two different satellites in a similar source state indicate an inhomogeneous corona, with decreasing temperature attributed to increasing height. Besides, utilising the broader energy coverage of *AstroSat*, we estimate the black hole mass to be $6.7 - 13.9 M_{\odot}$, consistent with independent measurements reported in the literature.

Key words: accretion, accretion discs — methods: data analysis — stars: black holes — X-rays: binaries — X-rays: individual: MAXI J1820+070

1 INTRODUCTION

Accreting black hole X-ray binaries are unique astrophysical laboratories to probe matter in extreme conditions. Based on the mass of the companion star, they can be classified into High Mass X-ray Binary (HMXB) and Low Mass X-ray Binary (LMXB). In black hole LMXBs, the main source of power is the gravitational energy released by matter accreted from the companion low mass star onto the black hole via Roche lobe overflow (e.g. Frank et al. (2002)). Based on the long-term temporal evolution of the X-ray emission, LMXBs can be further categorised into persistent and transient sources. Almost all black hole LMXBs are transients (Done et al. 2007). The transient LMXBs can be in a quiescent state for a long time, probably undetected until they go

into outbursts increasing intensities by few orders of magnitude. They exhibit various source states, such as Low Hard State (LHS), High Soft State (HSS) and High Intermediate state (HIS), which can be identified from the Hardness-Intensity Diagram (HID) (Belloni et al. 2000; Remillard & McClintock 2006a). The changes in the spectral states could be attributed to the change in the geometry of the accretion disc (Remillard & McClintock 2006a).

In terms of the X-ray spectrum, the HSS is dominated by a multi-colour black-body emission, attributed to the accretion disc. This is interpreted as the disc being very close to the innermost circular stable orbit (ISCO), leading to high disc temperatures (Belloni et al. 2000; Remillard & McClintock 2006a). On the other hand, the LHS is mainly dominated by a variable power-law component, with some hint of low-temperature disc component. The lower disc temperature is interpreted as the disc being truncated at a much larger radius (see, however, Reis et al. (2010)). The power-

★ E-mail: sudip.chakraborty@tifr.res.in (TIFR)

law component is generally attributed to a spatially compact region located above the central region of the accretion disc, named “corona” (Reynolds 2014). In this scenario, the hot corona irradiates the accretion disc, producing fluorescent and backscattered radiation. The re-emission from the irradiated disc is thought to be the (thermal) soft excess ~ 1 keV, broad iron line complex, and Compton hump around ~ 30 keV (Fabian 2016). In LHS, the Comptonising corona and the reflection from the disc give rise to the power-law continuum and reflection features, respectively. While in HSS, the corona weakens or disappears. Thus, LHS is dominated by power-law emission, whereas the HSS is dominated by the higher temperature disc emission. This interpretation of states and state transitions as changes in accretion disc geometry is being challenged in recent years. For example, Kara et al. (2019) have proposed the idea of contracting corona as opposed to changing disc truncation radius, as an explanation of states and state transitions. The exact geometry of the corona is still unclear. While a lamp-post geometry is often used for computational simplicity, this may not sufficiently reflect the actual scenario (Chauvin et al. 2018). Finally, Yamada et al. (2013), Basak et al. (2017) have proposed more general, inhomogeneous structure of the corona.

MAXI J1820+070 is a recently discovered bright X-ray transient, detected with Monitor of All-sky X-ray image, or *MAXI* (Matsuoka et al. 2009) on board the International Space Station (ISS) on 11th March 2018 at 12:50 UT (Kawamuro et al. 2018). Its optical counterpart, named ASSASN-2018ey, was observed with All-Sky Automated Survey for SuperNovae (ASAS-SN) (Tucker et al. 2018; Denisenko 2018). A consecutive *Swift* /BAT trigger led to a follow up monitoring of the source with XRT, which located the X-ray source at RA (J2000) = +18h 20m 21.88s and Dec (J2000) = +07d 11m 08.3s with an uncertainty of 1.5” (Kennea 2018).

During its 2018 outburst, the object was subsequently observed in multiple wavelengths: from radio (Bright et al. 2018; Trushkin et al. 2018), to infrared (Casella et al. 2018; Mandal et al. 2018), to optical (Baglio et al. 2018a; Littlefield 2018; Bahramian et al. 2018; Garnavich & Littlefield 2018; Sako et al. 2018a; Gandhi et al. 2018a). Optical observations (Baglio et al. 2018b) along with hard X-ray power-law spectrum, and large amplitude in the broadband power spectrum (Uttley et al. 2018) suggested that the source is a Black Hole Low mass X-ray Binary (BH LMXB). After the beginning of the outburst, MAXI J1820+070 underwent rapid increase in flux in both soft and hard X-rays, with hardness ratio remaining more or less constant (Del Santo & Segreto 2018b). Subsequent optical observations revealed an optical period of ~ 3.4 hr (Richmond 2018), as well as correlations between X-ray and optical brightness. (Paice et al. 2018, 2019; Townsend et al. 2018; Yu et al. 2018a). Further sub-millimetre detection (Tetarenko et al. 2018) and flat radio spectrum (Tetarenko et al. 2018) hinted the launch of a relativistic jet. After the initial rise in intensity, MAXI J1820+070 underwent a slow decay from around MJD 58200. The hard X-ray flux dropped sharply around MJD 53805, causing a state transition to the soft state. The source remained in the soft state for around 60 days before transiting back to the hard state around MJD 58390, before fading away into quiescence after MJD 58400 (Fig. 1).

During the LHS, MAXI J1820+070 had a hard spec-

trum with a photon index of ~ 1.5 (Del Santo & Segreto 2018a). Low-frequency quasi-periodic oscillations (QPOs) were detected in Optical and X-ray wavelengths (10-50 mHz) (Gandhi et al. 2018b; Mereminskiy et al. 2018; Yu et al. 2018b). Strong optical and X-ray short-term variabilities on time scales of less than 1 s were also reported (Gandhi et al. 2018b; Sako et al. 2018b). Kara et al. (2019) performed spectro-temporal study of MAXI J1820+070 and detected reverberation time lags between 0.1–1.0 keV and 1.0–10.0 keV energy bands. The authors have observed a corona height $< 5R_g$ and an inner disc radius $< 2R_g$ (where R_g is the gravitational radius of the black hole, defined as $R_g = GM/c^2$). They also claimed that with the evolution of the outburst the corona became compact and shifted close to the compact object. Spectral analysis during the LHS by Buisson et al. (2019) not only supported this claim but also suggested a correlation between X-ray luminosity and coronal temperature. However, a general relativistic simulation using the spectral analysis indicated that the spectral softening was due to the change in the inner disc radius rather than the coronal geometry (Roh 2020). The mass function of the binary system was reported to be $5.18 \pm 0.15 M_\odot$ (Torres et al. 2019). By constraining the inclination angle to be $69^\circ < i < 77^\circ$, the black hole mass was estimated to be $7-8 M_\odot$ (Torres et al. 2019). Using radio parallax method, Atri et al. (2020) estimated the accurate distance to the source to be 2.96 ± 0.33 kpc, further constraining the black hole mass of the source to $9.2 \pm 1.3 M_\odot$. Analysing the HSS spectra, Fabian et al. (2020) found the black hole mass to be $\sim 7-8 M_\odot$, and the black hole spin to be moderately low (dimensionless spin parameter, a , between -0.5 to $+0.5$). Using DR2 data of Gaia, Gandhi et al. (2019) found the source distance to be $3.46^{+2.18}_{-1.03}$ kpc. By analysing the soft X-ray data from NICER during the rising phase of outburst, Uttley et al. (2018) found the Galactic extinction (N_H) to be $1.5 \times 10^{21} \text{cm}^{-2}$.

In this work, we investigate the broadband spectral characteristics of the hard state spectra of MAXI J1820+070 during its 2018 outburst. We use the data from *AstroSat* observation during March 30-31, 2018 and a suitably chosen *NuSTAR* observation during March 24-25, 2018. The *AstroSat* spectra (without the Cadmium Zinc Telluride Imager (CZTI)) were presented with a simple model fit (and with greater systematic uncertainty assumed) in Mudambi et al. (2020). Of the broadband X-ray satellites currently available, *NuSTAR* and *AstroSat* provide good energy resolution in hard X-ray range (> 10 keV), with *AstroSat* covering a broader energy range. Here we utilise this opportunity, to systematically and uniformly study the broadband spectra of this BHXB from these independent satellite instruments using detailed spectral models for the first time. The paper is organised as follows. In section 2 we describe the data reduction procedure of *NuSTAR*, as well as all three pointing X-ray instruments on board *AstroSat*, namely Soft X-ray Telescope (SXT), The Large Area X-ray Proportional Counter (LAXPC) and CZTI. In section 2.5, we describe the *MAXI*/GSC and *Swift* /BAT lightcurves and HID generation. We then describe the states and state transition, as well as the *NuSTAR* data selection based on the mentioned HID in section 2.6. Furthermore, we present an in-depth spectral analysis of *NuSTAR* and *AstroSat* data in section 3.2.1 and 3.2.2, followed by an estimation of the black hole

Instrument	Obs ID (yyyy-mm-dd)	Obs. date	Exposure (s)
<i>NuSTAR</i>	90401309010	2018-03-24/25	2660
<i>AstroSat</i>	9000001994	2018-03-30/31	11768

Table 1. *NuSTAR* and *AstroSat* observation details. In case of *AstroSat*, we have mentioned only the SXT exposure time. The LAXPC and CZTI exposure times are higher by more than a factor of 2.

mass based on the same spectral fit in section 3.2.3. Finally, we summarise our results and discuss their implications in section 4.

2 OBSERVATION AND DATA REDUCTION

AstroSat, the first Indian dedicated astronomy satellite, was successfully launched on 2015 September 28, carrying five scientific instruments on board (Singh et al. 2014): the focusing Soft X-ray Telescope (SXT), Large Area X-ray Proportional Counters (LAXPCs, 3 units), the hard X-ray Cadmium Zinc Telluride Imager (CZTI), the all-sky monitor called Scanning Sky Monitor (SSM) and the Ultraviolet Imaging Telescopes (UVIT). *AstroSat* observed MAXI J1820+070 in a hard state during the outburst on 2018 March 30-31, and we use the data from all three X-ray instruments (SXT, LAXPC and CZTI) in the present work.

2.1 SXT

SXT (Singh et al. (2016, 2017)) is a grazing incidence X-ray telescope on board *AstroSat*, with a focal length of 2 m. It covers the energy range of 0.3-8 keV and has a field of view of $\sim 40'$ (Singh et al. 2014).

The SXT data are acquired in the PC mode and is significantly piled up. To minimise the effect of the pile-up, source spectrum is extracted from an annulus between $6'$ and $15'$ from the centre of the image (the details of the region selection for avoiding pile-up, are described in Appendix A). The deep blank sky background spectrum, provided by the instrument team¹, is used for the spectral modelling.

2.2 LAXPC

LAXPC (Yadav et al. 2016) is a proportional counter array on board *AstroSat* (Agrawal 2006; Singh et al. 2014) with a large effective area, which observes sources in Event Analysis (EA) mode with absolute time resolution of 10 μ s in the energy range of 3.0-80.0 keV. The extraction of lightcurve and spectrum from level 1 data is done by laxpcsoftv3.1² along with background lightcurve and background spectrum. Among the three units of LAXPC, we have considered only one unit. As LAXPC30 has gain instability issue caused by a gas leakage and LAXPC10 was showing unpredictable HV variations, the results reported in this paper are from

LAXPC20. We have also extracted lightcurves in different energy bands corresponding to *NuSTAR*, *Swift* /BAT and *MAXI*/GSC energies to plot HID as shown in Fig. 2.

2.3 CZTI

The level 1 data of *AstroSat* CZTI is reduced to level 2 cleaned events, spectra, and lightcurve using the tool *cztipipeline* of *cztipipeline* Ver 2.1³. The total light curve before background reduction is then checked for any instrumental anomalies near the South Atlantic Anomaly (SAA). The time intervals very close to the SAA, where a sharp increase in the count-rate is observed, are excluded. Only Quadrant 0 in CZTI is used for the spectrum, as the instrumental response features in the other quadrants are yet to be understood. Further, module 13 in Quadrant zero is excluded as with Lower Limit of Detection (LLD) at around 50 keV, it does not span the entire spectral region of interest from the CZTI in this particular case.

2.4 NuSTAR

MAXI J1820+070 was observed with *NuSTAR* (Harrison et al. 2013) during 2018 March 24-25 (the reasons of this data selection are detailed in section 3.1 and section 4). The *NuSTAR* data are processed using v.1.8.0 of the NuSTAR-DAS pipeline with *NuSTAR* CALDB v220171002. After filtering background flares due to enhanced solar activity by setting `saacalc = 2`, `saamode = OPTIMIZED`, and `tentacle = no` in NUPIPELINE, the effective exposure times are 2.6 and 2.8 ks for the two focal plane modules FPMA and FPMB, respectively. The source spectra are extracted from a circular region of the radius $180''$ centred on the source location. The background spectra are extracted from a blank region on the detector furthest from the source location to avoid source photons. The spectra are grouped in *ISIS* (Houck & Denicola 2000) version 1.6.2-41 to have a signal-to-noise ratio of at least 50 per bin, similar to Buisson et al. (2019).

2.5 MAXI/GSC and Swift /BAT Lightcurve

The Burst Alert Telescope on board Neil Gehrels *Swift* Observatory (*Swift* /BAT) and Gas Slit Camera on board Monitor of All-sky X-ray Image (*MAXI*/GSC) continuously traced the source throughout the outburst phase. The daily averaged lightcurves from *Swift* /BAT in 15 to 50 keV have been obtained from <https://swift.gsfc.nasa.gov/results/transients/> and is normalised by the Crab count-rate in *Swift* /BAT. A very sharp increase in flux is seen during the initial phase with a gradual decrease. Another peak is also seen around MJD 58300. For *MAXI*/GSC, <http://maxi.riken.jp> provided the lightcurves in 2-4 keV and 4-10 keV. The lightcurves are further normalised in respective bands by the Crab count-rate in *MAXI*/GSC. Further the hardness ratios are also obtained using the Crab normalised count-rates, the hard band being 4-10 keV and soft being 2-4 keV. A sharp rise is seen also in the *MAXI*/GSC (4-10 keV)

¹ https://www.tifr.res.in/~astrosat_sxt/index.html

² http://www.tifr.res.in/~astrosat_laxpc/LaxpcSoft_v1.0/antia/laxpcsoftv3.1_04Sept2019.tar.gz

³ http://astrosat-ssc.iucaa.in/?q=data_and_analysis

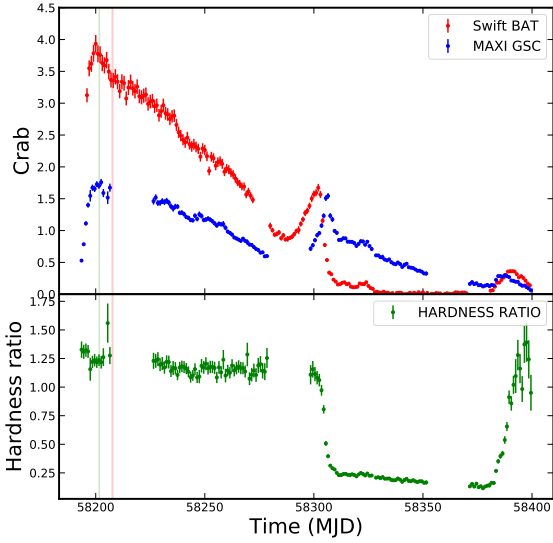


Figure 1. Upper panel : The red and blue points show the Crab normalised lightcurve of MAXI J1820+070 obtained using *Swift* /BAT and *MAXI*/GSC in energy range 15-50 keV and 4-10 keV. Lower panel: Crab normalised Hardness ratio (4-10 keV/2-4 keV) obtained using *MAXI*/GSC. The red and green vertical bands mark the epochs observed with *AstroSat* and *NuSTAR* , respectively.

during the initial phase but the hardness ratio remains constant. A sharp decrease is also observed around MJD 58300, and a further sharp rise is observed around MJD 58380. *AstroSat* and *NuSTAR* made pointed observations during the outburst marked by red and green vertical bands.

2.6 Hardness Intensity Diagram Generation from *MAXI*

The hardness intensity diagram (HID) for MAXI J1820+070 is been generated using daily monitoring data from *MAXI*/GSC (Fig. 2). For hardness ratio (Defined as the background-subtracted count-rate ratio in quoted energy bands), we choose 3.0-7.0 keV and 7.0-20.0 keV energy bands and consider intensity from 3.0 keV to 20.0 keV. Each point in the HID is averaged over one day. The pointed observations of the *AstroSat* (orange cross) and the *NuSTAR* (black square) reported in this paper are marked over the HID. The data from all three instruments are normalised by Crab counts, for a better comparison.

3 RESULTS

3.1 Spectral State and Transition

Most of the black hole X-ray binaries (BHXBs) are of transient nature and are discovered when outbursts occur. The evolution of an outburst in a BHXB is well depicted by a Hardness Intensity Diagram (HID) (Homan et al. 2001; Homan & Belloni 2005; Remillard & McClintock 2006b;

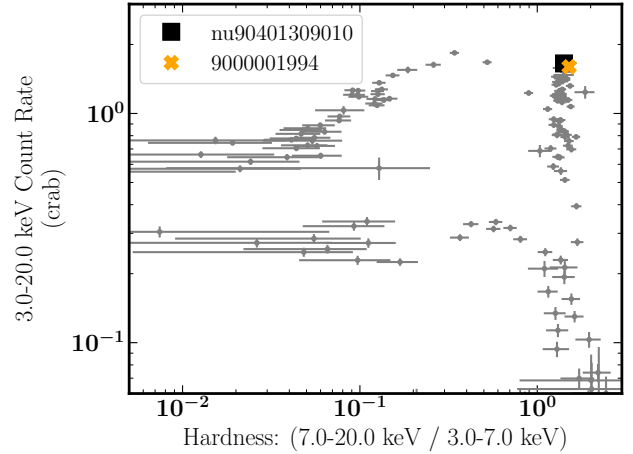


Figure 2. Hardness intensity diagram (HID) of MAXI J1820+070 with 1 day averaged *MAXI*/GSC monitoring observations during its first outburst. The scattered grey circles indicate the overall evolution of the source from MJD 58188 to MJD 58734. The *AstroSat* observation of interest is marked with an orange cross on the HID and the nearest *NuSTAR* observation which have consistent spectral properties is marked with a black square. The size of the error bars is similar to that of marker size for these two observations. See section 3.1 for a discussion on the HID.

Fender et al. 2009), which traces a ‘q-shaped’ trajectory moving in the counter clockwise direction. The best-known example is GX 339-4, which undergoes recurrent outbursts and has always followed a ‘q’ shaped path on HID (Belloni et al. 2005; Fender et al. 2009; Motta et al. 2011). The HID is a model-independent tool to study the state transitions in such BHXBs.

We generate the HID for MAXI J1820+070 (Fig. 2), using a daily monitoring *MAXI*/GSC data since the time of its discovery. The source has followed a ‘q’-shaped track similar to GX 339-4. Various states on HID, as described in section 1, are evident in Fig.2. We plot the *AstroSat* observation of our interest over the HID (orange cross), which is found to be in the hard state. During this state both hardness and intensity are high. We also considered one of the nearest *NuSTAR* observations (black square). The *NuSTAR* observation is also in a similar source hardness.

3.2 Spectral Analysis

The RMF files for SXT and LAXPC are obtained from the respective Payload Operation Center (POC) websites⁴. For SXT, sxt_pc_mat_g0to12.rmf is used as the RMF and sxt_pc_excl00_v04_20190608.arf is used as the ARF, whereas for LAXPC20 the response file lx20csh03v1.0.rmf is used. For joint fitting, both the SXT and LAXPC spectral files are binned in GRPPHA to have at least 30 counts per bin to facilitate χ^2 fitting. A 2% systematic uncertainty, as pre-

⁴ https://www.tifr.res.in/~astrosat_sxt/index.html

⁵ https://www.tifr.res.in/~astrosat_laxpc/

scribed by the instrument teams⁶, is used for the spectral fitting. For CZTI, the spectral and response files are generated using *czbindata* and *cztrspgen* of the *cztipipeline*⁷ respectively.

The spectral fitting and statistical analysis are carried out using the XSPEC version v-12.9.0n (Arnaud 1996). Energy ranges of 1.3-7.0 keV and 5-60 keV are used for SXT and LAXPC20 respectively. The photons below 1.3 keV and above 7.0 keV for SXT, and below 5.0 keV and above 60 keV for LAXPC, are ignored to avoid larger systematic errors. For CZTI, the energy range of 30 keV to 120 keV is used. Additionally, a gain correction is applied to the SXT data using the XSPEC command ‘gain fit’ with a slope of unity. The best fit offset value is found to be 34 eV and is used throughout the paper. For the joint fitting between different *AstroSat* instruments, a cross-normalisation constant (implemented using CONSTANT model in XSPEC) is allowed to vary freely for LAXPC and CZTI and is assumed to be unity for SXT. Similar cross-normalisation is considered between FPMA and FPMB for *NuSTAR* data fit. For *NuSTAR*, an energy range between 3 keV and 78 keV is considered for spectral fitting. To avoid the sharp instrumental features (as reported by Xu et al. (2018)), energies between 11-12 and 23-28 keV are excluded (Buisson et al. (2019)). All the models, as described below, include the Galactic absorption through the implementation of the TBABS model. The corresponding abundances are set in accordance with the Wilms et al. (2000) photoelectric cross-sections. The neutral hydrogen column density (N_{H}) is fixed to $1.5 \times 10^{21} \text{ cm}^{-2}$ (Uttley et al. 2018) for all the described models. All parameter uncertainties are reported at the 90% confidence level for one parameter of interest.

3.2.1 Spectral fits without reflection

First of all, to demonstrate the reflection features, we fit the *NuSTAR* spectra with an absorbed cutoff power-law model, TBABS×CUTOFFPL in XSPEC notation. For this, we only consider the energy intervals of 3-4, 8-12, and 40-78 keV, where reflection from the disc has minimal effect. As displayed in the second panel of Fig. 3, a broad iron Fe K- α emission with a narrow core, as well as a Compton hump peaking around 30 keV, are evident in the residuals. The slight difference ($\sim 1\%$) between FPMA and FPMB below 5 keV, is within the calibration accuracy of *NuSTAR* (Madsen et al. 2015).

For a better explanation of the observed broadband energy spectra, we fit the *NuSTAR* data with a model comprising of a combination of multicoloured disc black-body (diskbb: Mitsuda et al. (1984), Makishima et al. (1986)) and thermal Comptonisation (Nthcomp: Zdziarski et al. (1996), Życki et al. (1999)), TBABS×(DISKBB + NTHCOMP) in XSPEC notations. The seed photon temperature in NTHCOMP is set to the innermost temperature (T_{in}) of the DISKBB component. In the energy range mentioned before, we get

the best-fit DISKBB T_{in} to be $0.77_{-0.05}^{+0.06}$ keV, a power-law index (Γ) of 1.58 ± 0.01 , and the electron temperature kT_{e} to be 19.2 ± 0.3 keV. The fit results in a reduced χ^2/dof of 404.2/211. The value of the cross-normalisation factor between FPMA and FPMB is found to be 0.96 ± 0.01 ($\sim 4\%$), which is within the accepted limit of $\leq 5\%$ (Madsen et al. (2015), Marcotulli et al. (2017)). Due to the limited spectral coverage assumed here, the value of kT_{e} is somewhat low. To get a better fit and to explore the possibility of additional spectral components, we add another NTHCOMP model to the existing model. This double Comptonisation model gives a much better fit, with a χ^2/dof of 227.8/208. The fit results in a segregation of corona temperatures, with the best-fit kT_{e} being $27.4_{-2.3}^{+2.7}$ keV and $1.35_{-0.05}^{+0.02}$ keV. The T_{in} of the disc is found to be 0.42 ± 0.01 keV. Note that this exercise is for a demonstration purpose only and the derived values are unreliable/unphysical as these fits within narrow energy bands do not include the effect of reflection, which we will discuss in greater depth in section 3.2.2. In fact, the second Comptonisation component in this model could be fitting for the Compton hump of the reflection (though we have tried to avoid this by ignoring the corresponding energy range) rather than a true second Comptonisation. This shows the need for proper reflection modellings. Nevertheless, the important qualitative indication from this exercise is the possible existence of a second Comptonisation component, with a lower corona temperature.

Inspired by this result, we investigate the possibility of a double Comptonisation scenario in greater detail in section 3.2.2. Until now, we have not explored the reflection. In the following section, we perform an in-depth reflection modelling of both the *NuSTAR* and *AstroSat* broadband spectra.

3.2.2 Spectral fits with reflection

For a detailed investigation of the broadband spectra including the reflection features, we use the self-consistent relativistic disc reflection models from RELXILL model suite (relxill v1.2.0 : Dauser et al. (2014), García et al. (2014)). To minimise the number of free parameters, we assume a lamp-post geometry of the Comptonising corona and use the model RELXILLPCP which internally includes an NTHCOMP continuum. However, we only include the reflected flux from the RELXILLPCP component (by setting the model parameter refl_frac < 0). We add an explicit NTHCOMP component to represent the continuum. The seed photon temperature of the NTHCOMP component is tied to the inner accretion disc temperature (DISKBB T_{in}), and the electron temperatures (kT_{e}) and spectral indices (Γ) of both the NTHCOMP and RELXILLPCP components are tied together. As before, the value of N_{H} is fixed to $1.5 \times 10^{21} \text{ cm}^{-2}$, and the T_{in} from the additional DISKBB component is used as the seed temperature for the internal NTHCOMP continuum.

The inner radius (R_{in}) of the thin accretion disc, and the dimensionless black hole spin parameter (a), which are reflection spectrum parameters, are degenerate. For simplicity in spectral fitting, we assume a maximally spinning black hole ($a = 0.998$), and fit for R_{in} (for further discussion, refer to section 4). We fix the outer edge of the accretion disc (R_{out}) at $400R_{\text{g}}$ (where R_{g} is the gravitational

⁶ https://www.tifr.res.in/~astrosat_sxt/dataana_up/readme_sxt_arf_data_analysis.txt

⁷ http://astrosat-ssc.iucaa.in/uploads/czti/CZTI_level2_software_userguide_V2.1.pdf

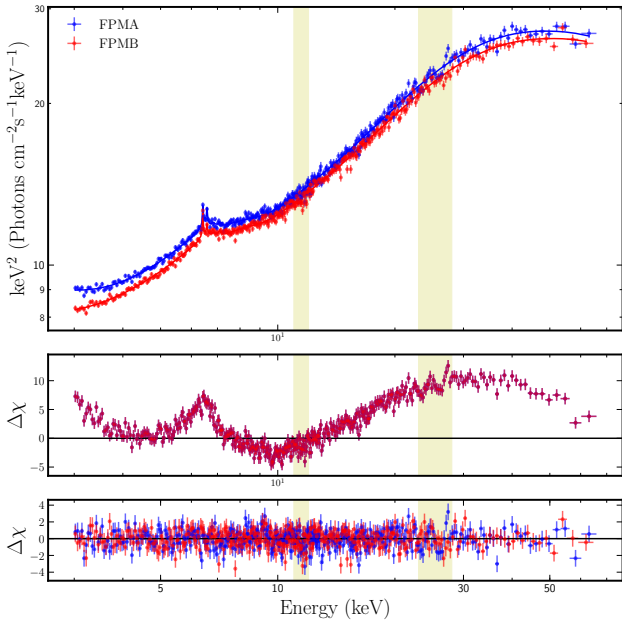


Figure 3. Results of 3-78 keV *NuSTAR* spectral fit of MAXI J1820+070 (see sections 3.2.2, 4 for further details). Top panel: the unfolded *NuSTAR* spectra. The blue and red points indicate FPMA and FPMB data, respectively. The spectra are folded with M2 model here. The yellow vertical bands denote the energy ranges ignored for spectral fitting due to instrumental features. Middle panel: The residuals of *NuSTAR* data, fitted with a fiducial TBABS×CUTOFFPL model. A soft excess, broad iron line and a Compton hump around ~30 keV are visible. Bottom panel: Residuals from M2 model fit.

radius of the black hole, defined as $R_g = GM/c^2$). On the other hand, we keep the inclination angle free (the data has sufficient signal for this purpose, as shown by Buisson et al. (2019)). The reflection fraction can thus be self-consistently determined by fitting R_{in} and the height of the lamp-post (h) from ray-tracing calculations (Dauser et al. 2014). To account for the narrow core of the Fe- $K\alpha$ line, we use the unblurred reflection model XILLVERCP (García & Kallman 2010). Similar to our implementation of RELXILLPCP, we use XILLVERCP only as a reflection component. The refl_frac of XILLVERCP is fixed at -1, as only insignificant variations are found in the subsequent fits if the refl_frac is allowed to vary freely. We tie the Γ and kT_e of the input continuum, as well as the iron abundances (A_{Fe}) and inclination angles (θ) of the RELXILLPCP and the XILLVERCP components. The ionisation parameters ($\xi = L/nR^2$, where L is the ionising continuum luminosity, R is the distance to the ionising source and n is the gas density) are allowed to be free for both the components. For XILLVERCP, we allow the $\log\xi$ to be non-zero, thus allowing for distant reprocessing by ionised gas. Thus, the total model setup is TBABS×(diskbb+Nthcomp(1)+relxillpCp(1)+xillverCp). This becomes our model M1 in table 2.

Inspired by the two Comptonisation scenario presented in section 3.2.2, we further add an additional NTHCOMP to the M1 model, reflected through the XILLVERCP component. For this purpose, we link the Γ and kT_e between the XILLVERCP and the new NTHCOMP compo-

nents. The seed temperature of the new NTHCOMP is again linked to the T_{in} of the DISKBB. Thus, the resulting model TBABS×(diskbb+Nthcomp(1)+relxillpCp(1)+xillverCp+Nthcomp(2)) becomes our model M2 in table 2.

To summarise, the two main models (in table 2) considered in our works are as follows:

- (i) TBABS×(diskbb+Nthcomp(1)+relxillpCp(1)+xillverCp): This forms the M1 model in table 2. Here, the NTHCOMP acts as the continuum, and the RELXILLPCP and XILLVERCP act solely as reflection, both reflecting the NTHCOMP component. The seed temperature of the NTHCOMP is tied to the DISKBB T_{in} , the kT_e and Γ of the NTHCOMP, RELXILLPCP and XILLVERCP are tied to each other. The A_{Fe} and θ , of the XILLVERCP are tied to that of RELXILLPCP component, while its ξ is allowed to vary freely. Basically, this model comprises of a single Comptonisation continuum being reflected from the disc by two different reflection components, one blurred and the other unblurred.
- (ii) TBABS×(diskbb+Nthcomp(1)+relxillpCp(1)+xillverCp+Nthcomp(2)): This makes the M2 model in table 2. Here, the NTHCOMP(1) acts as the hard/primary continuum, and the RELXILLPCP reflects the NTHCOMP(1) component. The seed temperature of the NTHCOMP(1) is tied to the DISKBB T_{in} , the kT_e and Γ of the NTHCOMP and RELXILLPCP are tied to each other. The NTHCOMP(2) component denotes the second, soft Comptonisation component; reflected by the XILLVERCP component. The seed temperature of the NTHCOMP(2) is tied to the DISKBB T_{in} , and the kT_e and Γ of the XILLVERCP are tied to that of the NTHCOMP(2) component. Just like in M1, the A_{Fe} and θ , of the XILLVERCP are tied to that of RELXILLPCP component, while its ξ is allowed to vary freely. More crucially, the kT_e and Γ of the two Comptonisation components are not tied to each other. Essentially, this model comprises of two Comptonisation continuum being reflected from the disc by two different reflection components, one blurred and the other unblurred, having different temperatures (and potentially two different lamp-post heights). This better mimics a realistic corona, allowing for a temperature structure.

To make a reasonable comparison with the *NuSTAR* spectral fit by Buisson et al. (2019), we allow the DISKBB T_{in} and normalisation, as well as the spectral index and normalisation of the intrinsic continuum to vary freely between FPMA and FPMB. This takes care of the slight calibration differences between the two modules. We find that apart from the DISKBB normalisation, the typical difference between the two modules in the other quantities are less than the stated calibration level (Madsen et al. 2015). The introduction of the reflection models vastly improves the goodness of fit. For model M1, the χ^2/dof is found to be 715.1/670. The innermost accretion disc temperature is observed to be $0.44^{+0.08}_{-0.07}$ keV, which is lower than the values reported by Buisson et al. (2019). However, we have to keep in mind that *NuSTAR* extends only up to 3.0 keV in lower energy side, and hence is not extremely suitable for accurate estimation of the accretion disc parameters on its own. Most of the other parameters, viz. Γ , R_{in} , $\log\xi$, A_{Fe} are found to be

consistent with the parameters in RELXILLPCP(1) model fit of epoch 3 spectra in Buisson et al. (2019). The values of Γ are consistent with hard state spectra of black hole X-ray binaries (Remillard & McClintock 2006a). Inner disc radius (R_{in} , of $6.9^{+0.9}_{-1.0} R_{\text{g}}$) extending very close to the Innermost Stable Circular Orbit (ISCO) and super-solar abundances (A_{Fe} of $4.4^{+1.3}_{-0.5}$ time solar) are also observed. The proximity of the inner radius of the disc to the ISCO is consistent with Kara et al. (2019); Buisson et al. (2019). The non-zero ionisation parameter ($\log \xi = 2.5^{+0.2}_{-0.1} \log[\text{erg.cm/s}]$) of the XILLVERCP indicates the presence of an ionised distant reflection component. However, the lamp-post height is found to be pegged near the lowermost allowable limit. The inclination angle is found to be 29^{+2}_{-8} degrees. Additionally, we observe a higher corona temperature (118^{+29}_{-19} keV) than the previously reported values. The best-fit parameter values are presented in the first column of table 2.

Addition of the second Comptonisation component improves the best-fit significantly. If the kT_{e} of the additional NTHCOMP is tied to that of the original RELXILLPCP component, the fit results in a χ^2/dof of 688.8/668. The common temperature of the corona is found to be 38^{+3}_{-2} keV. This value is similar to that obtained by Buisson et al. (2019), the implication of which is discussed later in this section and section 4. Now, if we untie the two kT_{e} components (thus forming model M2), the χ^2/dof becomes 666.1/667. The addition of the 3 free parameters change the best-fit values. All the disc reflection parameters, including the lamp-post height ($7.41^{+1.94}_{-1.93} R_{\text{g}}$), are found to be more or less consistent with the epoch 3 results from Buisson et al. (2019). The additional Comptonisation component is found to be at a much lower kT_{e} value of $14.0^{+2.1}_{-1.7}$ keV, as compared to 115^{+38}_{-29} keV of the primary Comptonisation component. The best-fit parameter values can be found in the second column in table 2. This segregation of the temperatures of the two coronal components hints towards the existence of an inhomogeneous corona. When the temperatures of the two components are tied, we get an average temperature of ~ 38 keV, which Buisson et al. (2019) found. An F -test between the fits with M1 and M2 model yields a very low false-positive probability of 2.9×10^{-10} , further solidifying the importance of the second Comptonisation component for obtaining a good fit. A detailed representation of the different spectral components can be found in Fig. 4 and the *NuSTAR* residual with M2 model fit is presented in the bottom panel in Fig. 3.

Similar to the *NuSTAR* spectral fits, we model the joint SXT+LAXPC+CZTI spectra. The broader energy range of 1.3-120.0 keV gives us a better handle over the disc parameters and high energy rollover, although the poorer spectral resolution around the iron lines gives a less reliable measurement of the reflection parameters. The best-fit parameters from M1 model fit are found to a little different than the contemporaneous *NuSTAR* fit. The inner disc temperature ($0.33^{+0.01}_{-0.01}$ keV) is found to be somewhat higher than the value reported in Mudambi et al. (2020), and close to the typical T_{in} values for the hard spectral state in black hole X-ray binaries (e.g. Wilkinson & Uttley (2009), Wang-Ji et al. (2018)). The spectral index $1.46^{+0.01}_{-0.01}$ is found to be somewhat lower than the *NuSTAR* values. The corona temperature (126^{+38}_{-7} keV) and ionisation param-

eter ($\log \xi = 3.69^{+0.03}_{-0.22} \log[\text{erg.cm/s}]$) are found to be close to the *NuSTAR* fit values. The lamp-post height ($4.1^{+0.7}_{-1.8} R_{\text{g}}$) is also found to be consistent with the Buisson et al. (2019) value. The *AstroSat* fit is also observed to prefer a closer inner disc. However, the iron abundance and the XILLVERCP ionisation parameter are pegged near the maximum allowed values. The maximality of the XILLVERCP ionisation parameter is most likely due to the limited spectral capability of LAXPC (more specifically, in LAXPC20), as discussed in section 4. Additionally, the LAXPC residual shows a peak at ~ 36 keV, which is not present in CZTI residual, indicating an instrumental origin. The feature can be attributed to Xenon K-edge and can be taken care of with the inclusion of a GAUSSIAN component (Sridhar et al. 2019). We found that a GAUSSIAN component of line energy ~ 35.9 keV and width $\sigma \sim 0.8$ keV sufficiently takes care of the feature. The resultant M1 model fit yields a χ^2/dof of 872.0/814.

Similar to *NuSTAR* M2 model fit, we add a second NTHCOMP component to the *AstroSat* M1 fit. The resultant M2 model fit yields a much better χ^2/dof of 856.8/8111. The best-fit *AstroSat* values are noted to be closer to the *NuSTAR* values for M2 model fit. The DISKBB temperature remains almost unchanged. The lamp-post height ($3.18^{+0.38}_{-0.47} R_{\text{g}}$) is found to be consistent with Kara et al. (2019). Similar to *NuSTAR*, the fit with the M2 model results in a much lower value of the kT_{e} of the second Comptonisation ($18.4^{+3.6}_{-3.2}$ keV), as opposed to the higher kT_{e} value (149^{+79}_{-33} keV) of the primary Comptonisation component. The iron abundance and the XILLVERCP ionisation parameter are still found to be pegged at the upper limit. The spectral index of the second NTHCOMP is found to be steeper ($1.57^{+0.01}_{-0.05}$) than the intrinsic Comptonisation component ($1.41^{+0.03}_{-0.04}$). The inner disc radius ($4.2^{+1.0}_{-0.9} R_{\text{ISCO}}$) also becomes comparable to the *NuSTAR* best-fit value. The best-fit parameter values for M1 and M2 fit are reported in the 3rd and 4th column in table 2. The spectra and the residuals can be found in Fig. 5. The high cross-normalisation factors between SXT and LAXPC/CZTI can be attributed to the small extraction area for SXT (explained in greater detail in appendix A). To further probe the effect of LAXPC on the significance of the second Comptonisation component, we fit the SXT+CZTI spectra between 1.3-5.0 keV and 40.0-120.0 keV with TBABSX(DISKBB+NTHCOMP) and TBABSX(DISKBB+NTHCOMP+NTHCOMP) models. The former fit results in a χ^2/dof of 1165.2/741, while the latter gives a χ^2/dof of 824.8/738. This further establishes the importance of the second Comptonisation component.

Finally, for a closer parallel to the *AstroSat* data with the published *NuSTAR* fits, we adopt a similar model to Buisson et al. (2019), involving a DISKBB and two RELXILLPCP components (denoted as RELXILLPCP(1) for the reflection component with lower height, and RELXILLPCP(2) for the higher corona). All the continuum parameters are allowed to vary freely. For simplicity, the inner disc radius is fixed at the ISCO. Thus, this model (M3: TBABSX(DISKBB+RELXILLPCP(1)+RELXILLPCP(2))) has two Comptonisation components at different heights, which are reflected from the inner disc. The resulting fit (model M3 in table 2) can be compared to M2 model fit, with a χ^2/dof of 861.4/818. The inclination angle is fixed at 30° , as allowing it to freely vary results in an unconstrained in-

clination value. The corona temperature shows a clear segregation, with a much higher temperature (150^{+9}_{-7} keV) for the corona closer to the black hole and a much lower temperature ($22.9^{+7.4}_{-4.3}$ keV) for the corona component further away. The temperature of the colder corona is somewhat consistent with *NuSTAR* and *AstroSat* M2 best-fit temperatures of the second Comptonisation component. The hotter corona (height of $2.8^{+0.8}_{-0.5}R_g$) component is also found to have higher ionisation parameter than the colder corona (height of $5.5^{+2.3}_{-1.2}R_g$) component. Note that, although the temperature structure is prominent, the segregation of lamp-post heights is not as pronounced as reported by Buisson et al. (2019).

3.2.3 Estimation of mass of the Black Hole

The inner accretion disc radius in a black hole LMXB can be measured either from fitting the disc or from modelling the disc reflection. Assuming the inner radii deduced from the DISKBB and RELXILLPCP components to be the same, we can derive the mass of the black hole (M_{BH}) from equation 3 in Wang et al. (2018). We use a correction factor of 1.2 (Kubota et al. 1998), accounting for the spectral hardening (Shimura & Takahara 1995) and the fact that the disc temperature does not peak at the inner radius (Makishima et al. 2000), see also equation 2 and the corresponding discussion in Reynolds & Miller (2013).

Using our best-fit values of R_{in} and DISKBB normalisation from a fit with the *AstroSat* model M2, as well as considering a distance estimate from Gandhi et al. (2019), we get the mass of the black hole in MAXI J1820+070 to be $6.7 - 13.9 M_{\odot}$. This mass estimate from our spectral model is consistent with the estimates from dynamical mass measurement from Torres et al. (2019) ($7 - 8 M_{\odot}$) and radio parallax measurement by Atri et al. (2020) ($9.2 \pm 1.3 M_{\odot}$). Additionally, this mass estimate from the hard state spectra is also consistent with the mass value derived from soft state spectra (Fabian et al. 2020).

4 DISCUSSIONS

In this paper, we report the results of broadband spectral analysis of 2018 hard state data of the transient black hole X-ray binary MAXI J1820+070 using all three pointing X-ray instruments (SXT, LAXPC and CZTI) on board *AstroSat*, as well as the nearest (both in time and in HID) available *NuSTAR* data. *NuSTAR* and *AstroSat* are the two most prominent currently active broadband X-ray satellites. While the *NuSTAR* data provides us with an opportunity to investigate the reflection features due to its superior energy resolution, the *AstroSat* data provides us a better handle over some other continuum parameters due to its much broader energy coverage between 1.3-120.0 keV. Thus, studying the source systematically in similar, contemporaneous states with the same models utilising two of the most prominent broadband instruments with such complementary capabilities, we derive conclusions that are more general and reliable. While the *NuSTAR* spectra are explored in great detail by Buisson et al. (2019), they tied the two coronal temperature. We show, in section 3.2.2, that this leads to a similar temperature even with our different

model implementation. We further show that a much more general assumption of untied temperatures between the two coronal components leads to a better fit and segregation of the two temperatures. Similarly, the *AstroSat* spectrum has been presented in Mudambi et al. (2020). However, it is used to get a rough understanding of the spectrum to help in their main aim of spectro-timing study. That apart, their spectra did not include CZTI, a better understanding of SXT pile-up, and not a very good fit even with 3% systematics (as opposed to the recommended 2% we have used). The DISKBB normalisation they derived, would imply to a black hole mass of 22–26 M_{\odot} , leading to inconsistent results. This motivated us to further explore the *AstroSat* data, with all three pointing X-ray instruments, in much greater detail.

The broadband spectra contains presence of soft excess, broad and narrow iron line complex and a Compton hump. The resultant spectrum is well fitted with the combination of a multi-colour disc black-body, a corona with a lamp-post geometry in the form of self-consistent, relativistic reflection model RELXILLPCP (which contains an intrinsic thermal Comptonisation continuum), and a distant, unblurred reflection component in the form of XILLVERCP. The resultant model, M1, is detailed in section 3.2.2 and table 2. From the best-fit *NuSTAR* spectra, we find the parameter values to be largely consistent with the previously reported values by Buisson et al. (2019) (epoch 3). The super-solar iron abundance of $4.4^{+1.3}_{-0.5}$ (relative to solar values) is also found to be consistent with the previous results. Similar overabundance of iron has been reported in various X-ray binaries (e.g. Degenaar et al. (2017), García et al. (2018), Tomsick et al. (2018)). The spectral index of the intrinsic NTHCOMP is found to be 1.54–1.55, typical of black hole X-ray binaries in the hard state. The distant reflection component is found to be ionised. The DISKBB T_{in} is found to be $\sim 0.42 - 0.45$ keV, which is lower than the previously reported value by Buisson et al. (2019). It is to be noted, however, that *NuSTAR* less reliable for the measurement of the DISKBB temperature and normalisation. Additionally, the *NuSTAR* data fit with the M1 model reveals a higher corona temperature (118^{+29}_{-19} keV) than previously reported. For the spectral characterisation of *AstroSat* data, we jointly fit the SXT (corrected for pile-up and appropriately gain shifted), LAXPC (LAXPC20) and CZTI data, utilising the full broadband capability of *AstroSat* between 1.3-120.0 keV. The *AstroSat* best-fit with M1 model indicates a lower but better constrained DISKBB T_{in} of $0.33^{+0.01}_{-0.01}$ keV, a similar corona temperature and ionisation parameter, and a somewhat lower spectral index.

We also explore the possibility of a two-component corona through the addition of an external NTHCOMP to our existing model. This implementation is similar in nature to the RELXILLPCP+RELXILLPCP scenario considered in Buisson et al. (2019), but has some key differences. Both the ionisation parameter and the electron temperature of the two Comptonisation components (the intrinsic NTHCOMP continuum of the RELXILLPCP model and the added NTHCOMP) are kept free and independent of each other. This gives us a more consistent and general picture, as the two components of the corona might have different physical properties. The inclusion of this additional Comptonisation component (the M2 model) vastly improves the goodness of fit for both *NuSTAR* and *AstroSat* data. In case of *NuSTAR*, tying up the temperature of the two coronal components

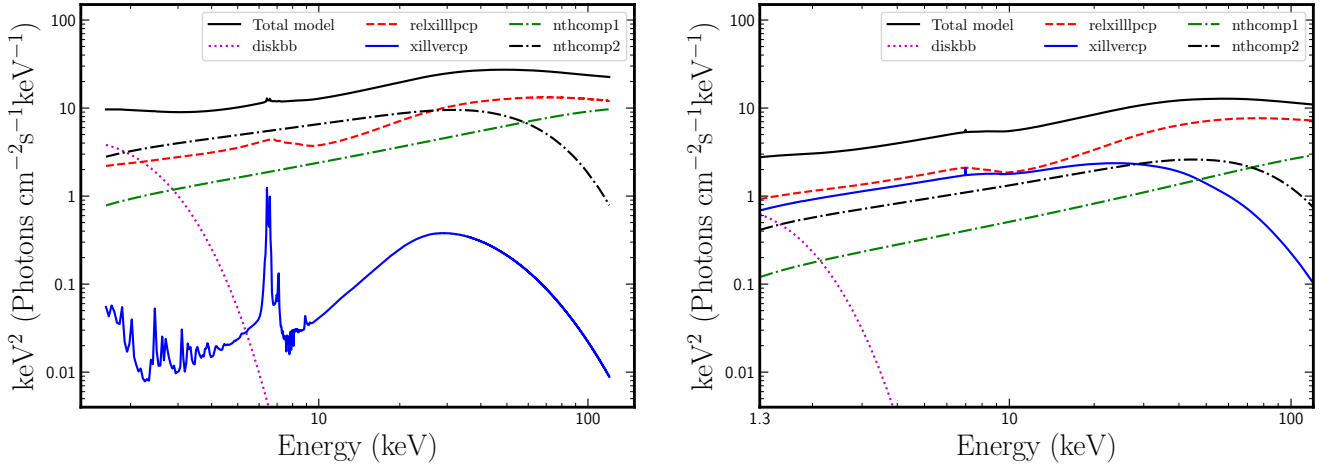


Figure 4. Best-fit M2 model for *NuSTAR* (left panel) and *AstroSat* (right panel). The dotted magenta curve corresponds to the multi-colour disc component. The dashed red curves and solid blue curves mark the RELXILLPCP and XILLVERCP components, respectively. The intrinsic NTHCOMP continua are represented by the green dash-dotted curves. The black dash-dotted curves indicate the second NTHCOMP Comptonisation components, with lower rollover energy. The spectral components are detailed in section 3.2.2, and the implications discussed in section 4.

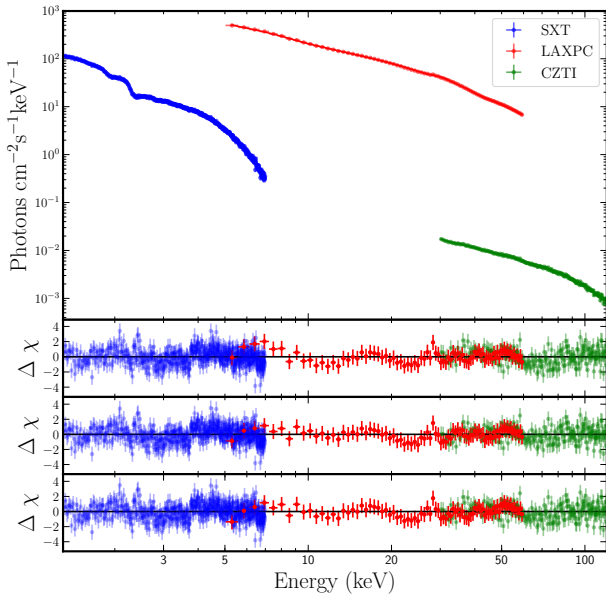


Figure 5. Results of 1.3-120 keV *AstroSat* spectral fit of MAXI J1820+070 (see sections 3.2.2, 4 for further details). Top panel: the *AstroSat* spectra. The blue, red and green points indicate SXT (1.3-7.0 keV), LAXPC (5-60 keV) and CZTI (30-120 keV) data, respectively. The spectra are fitted with M2 model here. The difference in normalisation between SXT and the rest of the instruments can be attributed to small region of extraction we used to avoid pile-up (detailed in section A). Second panel: Residuals from the M1 model fit. Third panel: Residuals from M2 model fit. Bottom panel: Residuals from M3 model fit.

leads to a kT_e of 38^{+3}_{-2} keV, consistent with Buisson et al. (2019). Untying the two temperatures and letting both vary freely; leads to a much better χ^2/dof than the previously reported models. The DISKBB T_{in} is almost unaffected by the inclusion of this added component, and the other best-fit parameters are broadly consistent between *NuSTAR* and *AstroSat*. For both *NuSTAR* and *AstroSat*, the height of the lamp-post corona is found to be consistent with Kara et al. (2019). Letting both the corona temperatures free, leads to a segregation of temperatures for both *NuSTAR* and *AstroSat*. While the temperature of the primary Comptonisation component is found to be 115^{+38}_{-29} keV and 149^{+79}_{-33} keV, the kT_e of the second Comptonisation component is found to be $14.0^{+2.1}_{-1.7}$ keV and $18.4^{+3.6}_{-3.2}$ keV for *NuSTAR* and *AstroSat* data, respectively. This difference in corona temperatures can be interpreted as originating from different distances from the black hole. The high energy corona is much closer to the black hole, has a higher electron temperature and contributes to the broad iron line through blurred reflection; while the low energy corona is further away, has much lesser electron temperature and contributes to the narrow core of the iron line complex. Similar interpretation of inhomogeneous corona has been used for Cyg X-1 (Yamada et al. (2013), Basak et al. (2017)). This idea is further reinforced by the implementation of our M3 model in table 2, where for *AstroSat* data we used a model almost similar to Buisson et al. (2019), with both the corona reflecting for a disc extending upto the ISCO and the continuum parameters of the two corona allowed to vary freely. This leads to a separation in both temperature and (to a certain extent) height, with the corona further away (RELXILLPCP(2)) having lower ionisation and temperature than the corona closer to the back hole (RELXILLPCP(1)). Note that this interpretation, though a little different, is not inconsistent with the contracting corona scenario (Kara et al. 2019); it just assigns a more realistic temperature structure to the corona. This also shows that tying up the temperatures of the higher and

lower temperature corona leads to an average temperature, similar to the one found by [Buisson et al. \(2019\)](#).

A few points are to be noted about the fits described in our work. First of all, by setting the RELXILLPCP and XILLVERCP `refl_frac < 0` (thereby including only the reflected flux from the respective components), we attempt to avoid the possibility of the second reflection component adding significantly to the continuum (and hence mimicking the spectra for a second corona temperature), rather than only fitting the reflection features (iron line, Compton hump etc.). The similarity in the best-fit parameters for *NuSTAR* and *AstroSat*, and the likelihood of the second Comptonisation with a similar temperature for both the instruments provide a further credence to our claim of a multi-temperature corona. That apart, the M3 model fit of *AstroSat* data provides further support that the two different temperatures can be attributed to different corona heights. Nevertheless, the alternate scenario (only one temperature and second reflection component adding to the continuum) cannot be entirely ruled out.

As XILLVERCP corresponds to a corona situated farther away, this component should be less ionised than the RELXILLPCP component. This is what we find for *NuSTAR* fits (see Table 2). However, the XILLVERCP ionisation parameter, for *AstroSat* fits, is pegged to a maximal value, and is higher than the best-fit value of the RELXILLPCP ionization parameter (see Table 2). This higher value could be because *AstroSat* (LAXPC20, in particular) cannot adequately describe the narrow features of XILLVERCP (see Fig. 4) due to a limited spectral capability. However, the XILLVERCP component is necessary even for *AstroSat* fits. We conclude this, because, while the χ^2/dof is 856.8/811 for the model M2, it is 885.1/814 if XILLVERCP is excluded from M2. Note that, if we force a lower value of the XILLVERCP ionisation parameter, by tying it to the RELXILLPCP ionisation parameter for the M2 model of *AstroSat* fitting, the contribution of the XILLVERCP component becomes negligible, and the fit is much worse with $\chi^2/\text{dof} = 886.4/813$. Nevertheless, the best-fit parameter values (e.g., DISKBB $T_{\text{in}} = 0.29^{+0.01}_{-0.01}$ keV) for this modified M2 model are overall consistent with those for the M2 model for *AstroSat* fitting. Moreover, the fits of both *AstroSat* and *NuSTAR* spectra with the M2 model give a similar conclusion, e.g., a temperature structure of the corona. These give confidence to our results, and we list the best-fit parameter values for the *AstroSat* M2 model fit in Table 2, although *AstroSat* cannot adequately model the XILLVERCP component.

The R_{in} for both *NuSTAR* and *AstroSat* are found to be of similar values ($5.4^{+1.5}_{-1.5} R_g$ for *NuSTAR*, and $4.2^{+1.0}_{-0.9} R_g$ for *AstroSat* for M2 model fit; see Table 2). For a maximally spinning black hole, this would place the inner edge of the accretion disc at $2.7 - 5.6 R_{\text{ISCO}}$ (R_{ISCO} : radius of the innermost stable circular orbit). However, this does not necessarily imply a truncated disc, as R_{in} and a are degenerate and we fix the dimensionless spin parameter (a) to 0.998, only to simplify a stable fitting process (section 3.2.2). Note that R_{ISCO} is determined by the black hole spin, and it monotonically increases from $1.24 R_g$ for an extremely prograde spinning black hole to $9.0 R_g$ for an extremely retrograde spinning black hole. The alternate scenario of a low black hole spin with a disc extending all the way down to ISCO, is equally likely, and the spectral fitting alone may be in-

sufficient to distinguish between different a -values. In fact, the almost unchanging R_{in} from [Kara et al. \(2019\)](#) and the consistency of best-fit R_{in} throughout the 8 epoch in [Buisson et al. \(2019\)](#) imply that R_{in} does not vary much throughout the outburst. Furthermore, the soft state spectral fitting by [Fabian et al. \(2020\)](#) supports a spin value between -0.5 and $+0.5$. Both these evidences indicate that MAXI J1820+070 may contain a low spin black hole, with the disc extending to ISCO. To test if our best-fit parameter values allow this possibility, we fix the R_{in} to the ISCO radius, make the spin parameter a free, fix the inclination at 30° , and freeze all the other parameters (except the normalisations) to their best-fit values in the M2 model fit of *NuSTAR* data. This results in an acceptable fit, with a χ^2 of 672.0 for 678 degrees of freedom. The corresponding best-fit spin parameter is $0.48^{+0.25}_{-0.26}$, which is consistent with [Fabian et al. \(2020\)](#).

Finally, assuming the same inner disc radius between the DISKBB and RELXILLPCP, we calculate the mass of the black hole to be $6.7 - 13.9 M_\odot$, consistent with previously reported values. This is the first time the mass of this black hole has been calculated from the hard state spectra in such a way. It is to be noted that most studies deriving the color-correction factor have involved BHXBs predominantly in soft state (see [Reynolds & Miller \(2013\)](#); [Merloni et al. \(2000\)](#) for exceptions), and a higher value might be warranted in hard states ([Reynolds & Miller 2013](#); [Dunn et al. 2011](#); [Davis & El-Abd 2019](#)). The consistency of the black hole mass estimate through this method with the other values, however, can provide a justification towards a disc origin of the thermal emission (as opposed to a reflection origin). This is further corroborated by [Fabian et al. \(2020\)](#).

From our best-fit model (M2), we find the unabsorbed 0.1-500 keV flux to be $1.64 - 1.69 \times 10^{-7}$ erg/cm²/s for the *NuSTAR* data and $1.62 - 1.64 \times 10^{-7}$ erg/cm²/s for the *AstroSat* data. This implies a 0.1-500 keV luminosity of $L_{0.1-500 \text{ keV}} \sim 2.32 - 2.42 \times 10^{38}$ erg/s. This implies that the black hole in MAXI J1820+070 is accreting at 13–29% L_{Edd} .

To summarise, through systematic investigation of contemporaneous *AstroSat* and *NuSTAR* data in similar states and with similar models, we have characterised the broadband X-ray spectra of the transient black hole X-ray binary MAXI J1820+070 in the hard state (March 2018) during its 2018 outburst. The *NuSTAR* best-fit parameters are found to be largely consistent with the values reported in the literature. We also fully utilise the broadband capability of all the pointing X-ray instruments on board *AstroSat*, through consistent spectral analysis in 1.3-120.0 keV energy range. Though there are some quantitative differences of the best-fit parameters between *NuSTAR* and *AstroSat*, the broad conclusions are consistent with each other. The inclusion of *AstroSat* data complements the *NuSTAR* data, as *NuSTAR* spectral fit gives us a better estimate of the reflection parameters, while *AstroSat* data provides superior estimates of disc temperature, normalisation and the high energy rollover of the corona. We utilise this potential to also investigate the possibility of an inhomogeneous corona through the implementation of a double Comptonisation model, which leads to better goodness of fit for both *NuSTAR* and *AstroSat* data. The consistency of the low energy Comptonisation component for independent observations with different instruments in a similar state (with *AstroSat* covering a broader energy range) establishes the significance of our results.

Table 2. Parameters of fits to MAXI J1820+070 spectra in the hard state observations with *AstroSat* and *NuSTAR*. The models M1, M2 and M3 are detailed in section 3.2.2. Errors represent 90% confidence intervals. f denotes that the corresponding parameter is frozen. P or p denotes that the parameter is pegged at the upper/lower limit value.

Spectral Component	Parameter	<i>NuSTAR</i>		<i>AstroSat</i>		
		M1	M2	M1	M2	M3
diskbb	kT_{in} (keV)	$0.44^{+0.08}_{-0.07}$ (FPMA)	$0.45^{+0.06}_{-0.05}$ (FPMA)	$0.33^{+0.01}_{-0.01}$	$0.31^{+0.01}_{-0.01}$	$0.35^{+0.01}_{-0.01}$
		$0.42^{+0.09}_{-0.08}$ (FPMB)	$0.43^{+0.05}_{-0.05}$ (FPMB)			
	norm ($\times 10^4$)	$2.25^{+4.37}_{-0.99}$ (FPMA)	$1.74^{+7.54}_{-0.44}$ (FPMA)	$1.39^{+0.36}_{-0.26}$	$1.62^{+0.49}_{-0.35}$	$1.21^{+0.34}_{-0.24}$
		$2.02^{+21.4}_{-1.13}$ (FPMB)	$1.67^{+1.26}_{-0.42}$ (FPMB)			
Nthcomp(1)	Γ	$1.54^{+0.01}_{-0.01}$ (FPMA)	$1.49^{+0.03}_{-0.04}$ (FPMA)	$1.46^{+0.01}_{-0.01}$	$1.41^{+0.03}_{-0.04}$...
		$1.54^{+0.01}_{-0.01}$ (FPMB)	$1.49^{+0.02}_{-0.08}$ (FPMB)			
	kT_e (keV)	118^{+29}_{-19}	115^{+38}_{-29}	126^{+38}_{-7}	149^{+79}_{-33}	...
relxilllpCp(1) (lower reflection)	Γ	$1.38^{+0.01}_{-0.01}$
	kT_e (keV)	150^{+9}_{-7}
	h (R_g)	< 2.8	$7.41^{+1.94}_{-1.93}$	$4.1^{+0.7}_{-1.8}$	$3.2^{+0.4}_{-0.5}$	$2.8^{+0.8}_{-0.5}$
	θ ($^\circ$)	29^{+2}_{-8}	25^{+8}_{-2}	27^{+8}_{-10}	35^{+7}_{-9}	30^f
	R_{in} (R_g)	$6.9^{+0.9}_{-1.0}$	$5.4^{+1.5}_{-1.5}$	$2.5^{+1.2}_{-1.0}$	$4.2^{+1.0}_{-0.9}$	1.2^f
	$\log \xi$ (log[erg cm/s])	$3.9^{+0.2}_{-0.1}$	$3.38^{+0.04}_{-0.03}$	$3.69^{+0.03}_{-0.22}$	$3.68^{+0.03}_{-0.13}$	$4.21^{+0.01}_{-0.01}$
	A_{Fe} ($A_{\text{Fe},\odot}$)	$4.4^{+1.3}_{-0.5}$	$5.0^{+0.3}_{-0.2}$	10.0^P	10.0^P	10.0^P
	\mathcal{R}	0.54	1.21	1.93	1.30	2.42
	norm	1.96 (FPMA) 1.70 (FPMB)	0.09 (FPMA) 0.08 (FPMB)	0.05	0.12	0.16
xillverCp	$\log \xi$ (log[erg cm/s])	$2.5^{+0.2}_{-0.1}$	$2.4^{+0.1}_{-0.2}$	4.70^P	4.70^P	...
	norm ($\times 10^{-2}$)	1.4	0.4	2.36	1.16	...
Nthcomp(2)	Γ	...	$1.66^{+0.02}_{-0.02}$...	$1.57^{+0.01}_{-0.05}$...
	kT_e (keV)	...	$14.0^{+2.1}_{-1.7}$...	$18.4^{+3.6}_{-3.2}$...
	norm	...	2.17	...	0.40	...
relxilllpCp(2) (upper reflection)	h (R_g)	$5.5^{+2.3}_{-1.2}$
	Γ	$1.44^{+0.01}_{-0.01}$
	kT_e (keV)	$22.9^{+7.4}_{-4.3}$
	$\log \xi$ (log[erg cm/s])	$3.62^{+0.09}_{-0.07}$
	\mathcal{R}	1.92
	norm	0.01
$\chi^2/\text{d.o.f.}$		715.1/670	666.1/667	872.0/814	856.8/811	861.4/818
	C_{LAXPC}	1.95	1.95	1.93
	C_{CZTI}	1.94	1.94	1.93
	C_{FPMB}	0.96	0.96
Unabsorbed flux	3.0–70.0 keV	8.9	8.9	7.8	7.8	7.8

Note: T_{in} : Temperature of the inner disc; norm: Normalisation of the corresponding spectral parameter; Γ : Asymptotic power-law photon index; T_e : Electron temperature of the corona, determining the high energy rollover; h : Height of the comptonising lamp-post corona above the black hole; θ : Inclination of the inner disc; R_{in} : Inner disc radius (in units of R_g); ξ : Ionisation parameter of the accretion disc, defined as $\xi = L/nR^2$, with L , n , R being the ionising luminosity, gas density and the distance to the ionised source, respectively; A_{Fe} : Iron abundance, in the units of solar abundance; \mathcal{R} : Reflection fraction; C_{LAXPC} : the flux normalisation constant for LAXPC (determined by multiplicative ‘constant’ parameter in the spectral models) is estimated with respect to the SXT flux. Similarly, we have denoted C_{CZTI} for CZTI flux normalisation constant with respect to the SXT flux, and C_{FPMB} for FPMB flux normalisation constant with respect to the FPMA flux.

MNRAS **000**, 1–14 (2015)

ACKNOWLEDGEMENTS

We thank the referee for constructive comments, which improved the paper. We also acknowledge the supports from Indian Space Research Organisation (ISRO) for mission operations and distributions of the data through ISSDC. This work has used the data from the Soft X-ray Telescope (SXT) developed at TIFR, Mumbai, and the SXT Payload Operations Center (POC) at TIFR is thanked for verifying and releasing the data via the ISSDC data archive and providing the necessary software tools. The LAXPC POC, TIFR, Mumbai is also acknowledged for providing us important inputs and necessary tools for data analysis. This research has made use of the *MAXI* data provided by RIKEN, JAXA and the *MAXI* team. This research has also made use of the *NuSTAR* Data Analysis Software (NuSTARDAS), jointly developed by the ASI Science Data Center (ASDC, Italy) and the California Institute of Technology (USA). The authors also thank Dr. Sunil Chandra for valuable insights and comments regarding SXT pile-up correction.

DATA AVAILABILITY

The observational data used in this paper are publicly available at NASA's High Energy Astrophysics Science Archive Research Center (HEASARC; <https://heasarc.gsfc.nasa.gov/>) and ISRO's Science Data Archive for AstroSat Mission (https://astrobrowse.issdc.gov.in/astro_archive/archive/Home.jsp), and references are mentioned. Any additional information will be available upon reasonable request.

REFERENCES

- Agrawal P. C., 2006, *Advances in Space Research*, **38**, 2989
 Arnaud K. A., 1996, XSPEC: The First Ten Years. p. 17
 Atri P., et al., 2020, *MNRAS*, **493**, L81
 Baglio M. C., Russell D. M., Lewis F., 2018a, The Astronomer's Telegram, **11418**, 1
 Baglio M. C., Russell D. M., Lewis F., 2018b, The Astronomer's Telegram, **11418**, 1
 Bahramian A., Strader J., Dage K., 2018, The Astronomer's Telegram, **11424**, 1
 Basak R., Zdziarski A. A., Parker M., Islam N., 2017, *MNRAS*, **472**, 4220
 Belloni T., Klein-Wolt M., Méndez M., van der Klis M., van Paradijs J., 2000, *A&A*, **355**, 271
 Belloni T., Homan J., Casella P., van der Klis M., Nespoli E., Lewin W. H. G., Miller J. M., Méndez M., 2005, *A&A*, **440**, 207
 Bright J., Fender R., Motta S., 2018, The Astronomer's Telegram, **11420**, 1
 Buisson D. J. K., et al., 2019, *MNRAS*, **490**, 1350
 Casella P., Vincentelli F., O'Brien K., Testa V., Maccarone T. J., Uttley P., Fender R., Russell D. M., 2018, The Astronomer's Telegram, **11451**, 1
 Chauvin M., et al., 2018, *Nature Astronomy*, **2**, 652
 Dauser T., Garcia J., Parker M. L., Fabian A. C., Wilms J., 2014, *MNRAS*, **444**, L100
 Davis S. W., El-Abd S., 2019, *ApJ*, **874**, 23
 Degenaar N., Pinto C., Miller J. M., Wijnands R., Altamirano D., Paerels F., Fabian A. C., Chakraborty D., 2017, *MNRAS*, **464**, 398
 Del Santo M., Segreto A., 2018a, The Astronomer's Telegram, **11427**
 Del Santo M., Segreto A., 2018b, The Astronomer's Telegram, **11427**, 1
 Denisenko D., 2018, The Astronomer's Telegram, **11400**, 1
 Done C., Gierliński M., Kubota A., 2007, *A&ARv*, **15**, 1
 Dunn R. J. H., Fender R. P., Körding E. G., Belloni T., Merloni A., 2011, *MNRAS*, **411**, 337
 Fabian A. C., 2016, *Astronomische Nachrichten*, **337**, 375
 Fabian A. C., et al., 2020, *MNRAS*,
 Fender R. P., Homan J., Belloni T. M., 2009, *MNRAS*, **396**, 1370
 Frank J., King A., Raine D. J., 2002, *Accretion Power in Astrophysics: Third Edition*
 Gandhi P., Paice J. A., Littlefair S. P., Dhillon V. S., Chote P., Marsh T. R., 2018a, The Astronomer's Telegram, **11437**, 1
 Gandhi P., Paice J. A., Littlefair S. P., Dhillon V. S., Chote P., Marsh T. R., 2018b, The Astronomer's Telegram, **11437**, 1
 Gandhi P., Rao A., Johnson M. A. C., Paice J. A., Maccarone T. J., 2019, *MNRAS*, **485**, 2642
 García J., Kallman T. R., 2010, *ApJ*, **718**, 695
 García J., et al., 2014, *ApJ*, **782**, 76
 García J. A., et al., 2018, *ApJ*, **864**, 25
 Garnavich P., Littlefield C., 2018, The Astronomer's Telegram, **11425**, 1
 Harrison F. A., et al., 2013, *ApJ*, **770**, 103
 Homan J., Belloni T., 2005, *Ap&SS*, **300**, 107
 Homan J., Wijnands R., van der Klis M., Belloni T., van Paradijs J., Klein-Wolt M., Fender R., Méndez M., 2001, *ApJS*, **132**, 377
 Houck J. C., Denicola L. A., 2000, *ISIS: An Interactive Spectral Interpretation System for High Resolution X-Ray Spectroscopy*. p. 591
 Kara E., et al., 2019, *Nature*, **565**, 198
 Kawamuro T., et al., 2018, The Astronomer's Telegram, **11399**, 1
 Kennea J. A., 2018, The Astronomer's Telegram, **11406**, 1
 Kubota A., Tanaka Y., Makishima K., Ueda Y., Dotani T., Inoue H., Yamaoka K., 1998, *PASJ*, **50**, 667
 Littlefield C., 2018, The Astronomer's Telegram, **11421**, 1
 Madsen K. K., et al., 2015, *ApJS*, **220**, 8
 Makishima K., Maejima Y., Mitsuda K., Bradt H. V., Remillard R. A., Tuohy I. R., Hoshi R., Nakagawa M., 1986, *ApJ*, **308**, 635
 Makishima K., et al., 2000, *ApJ*, **535**, 632
 Mandal A. K., Singh A., Stalin C. S., Chandra S., Gandhi P., 2018, The Astronomer's Telegram, **11458**, 1
 Marcotulli L., et al., 2017, *ApJ*, **839**, 96
 Matsuoka M., et al., 2009, *PASJ*, **61**, 999
 Mereminskiy I. A., Grebenev S. A., Molkov S. V., Zaznubin I. A., Khorunzhev G. A., Burenin R. A., Eseevich M. V., 2018, The Astronomer's Telegram, **11488**, 1
 Merloni A., Fabian A. C., Ross R. R., 2000, *MNRAS*, **313**, 193
 Mitsuda K., et al., 1984, *PASJ*, **36**, 741
 Motta S., Muñoz-Darias T., Casella P., Belloni T., Homan J., 2011, *MNRAS*, **418**, 2292
 Mudambi S. P., Maqbool B., Misra R., Hebbar S., Yadav J. S., Gudennavar S. B., S. G. B., 2020, *ApJ*, **889**, L17
 Paice J. A., Gandhi P., Page K., Altamirano D., Court J., Charles P., 2018, The Astronomer's Telegram, **11432**, 1
 Paice J. A., et al., 2019, *MNRAS*, **490**, L62
 Reis R. C., Fabian A. C., Miller J. M., 2010, *MNRAS*, **402**, 836
 Remillard R. A., McClintock J. E., 2006a, *ARA&A*, **44**, 49
 Remillard R. A., McClintock J. E., 2006b, *ARA&A*, **44**, 49
 Reynolds C. S., 2014, *Space Sci. Rev.*, **183**, 277
 Reynolds M. T., Miller J. M., 2013, *ApJ*, **769**, 16
 Richmond M., 2018, The Astronomer's Telegram, **11596**, 1
 Roh J., 2020, in *American Astronomical Society Meeting Abstracts*. p. 379.02
 Romano P., et al., 2006, *A&A*, **456**, 917

- Sako S., Ohsawa R., Ichiki M., Maehara H., Morii M., Tanaka M., 2018a, *The Astronomer's Telegram*, **11426**, 1
- Sako S., Ohsawa R., Ichiki M., Maehara H., Morii M., Tanaka M., 2018b, *The Astronomer's Telegram*, **11426**, 1
- Shimura T., Takahara F., 1995, *ApJ*, **445**, 780
- Singh K. P., et al., 2014, in *Space Telescopes and Instrumentation 2014: Ultraviolet to Gamma Ray*. p. 91441S, doi:10.1117/12.2062667
- Singh K. P., et al., 2016, In-orbit performance of SXT aboard AstroSat. p. 99051E, doi:10.1117/12.2235309
- Singh K. P., et al., 2017, *Journal of Astrophysics and Astronomy*, **38**, 29
- Sridhar N., Bhattacharyya S., Chandra S., Antia H. M., 2019, *MNRAS*, **487**, 4221
- Tetarenko A. J., Bremer M., Bright J., Sivakoff G. R., Miller-Jones J. C. A., Russell T. D., Japcot Xrb Collaboration 2018, *The Astronomer's Telegram*, **11440**, 1
- Tomsick J. A., et al., 2018, *ApJ*, **855**, 3
- Torres M. A. P., Casares J., Jiménez-Ibarra F., Muñoz-Darias T., Armas Padilla M., Jonker P. G., Heida M., 2019, *ApJ*, **882**, L21
- Townsend A., et al., 2018, *The Astronomer's Telegram*, **11574**, 1
- Trushkin S. A., Nizhelskij N. A., Tsybulev P. G., Erkenov A., 2018, *The Astronomer's Telegram*, **11439**
- Tucker M. A., et al., 2018, *ApJ*, **867**, L9
- Uttley P., et al., 2018, *The Astronomer's Telegram*, **11423**, 1
- Wang-Ji J., et al., 2018, *ApJ*, **855**, 61
- Wang Y., Méndez M., Altamirano D., Court J., Beri A., Cheng Z., 2018, *MNRAS*, **478**, 4837
- Wilkinson T., Uttley P., 2009, *MNRAS*, **397**, 666
- Wilms J., Allen A., McCray R., 2000, *ApJ*, **542**, 914
- Xu Y., et al., 2018, *ApJ*, **852**, L34
- Yadav J. S., et al., 2016, *ApJ*, **833**, 27
- Yamada S., Makishima K., Done C., Torii S., Noda H., Sakurai S., 2013, *PASJ*, **65**, 80
- Yu W., Zhang J., Yan Z., Wang X., Bai J., 2018a, *The Astronomer's Telegram*, **11510**, 1
- Yu W., Zhang J., Yan Z., Wang X., Bai J., 2018b, *The Astronomer's Telegram*, **11510**, 1
- Zdziarski A. A., Johnson W. N., Magdziarz P., 1996, *MNRAS*, **283**, 193
- Życki P. T., Done C., Smith D. A., 1999, *MNRAS*, **309**, 561

APPENDIX A: PILE-UP CHECK

The SXT PC mode data for MAXI J1820+070, taken at a time when the source flux is >1 Crab, is found to be highly piled up. In order to investigate and rectify the pile-up effect, we fit the 1.3-5.0 keV SXT data with a TBABS \times (DISKBB+NTHCOMP) model, avoiding the Fe K- α complex. The N_H is fixed to 1.5×10^{21} cm $^{-2}$, as used in the rest of the work, and the NTHCOMP seed temperature is set at the T_{in} of the DISKBB component. This model is applied to different groups of SXT data, each group differing from previous one by the greater amount of area of the central bright region excluded from the source PSF on the SXT CCD., with the outer edge of the selected annular regions fixed at $15'$. Similar to the procedure in Romano et al. (2006), it is noted that the spectra become steeper as more area is excluded until it reaches a stable value. The radius from the centroid of the PSF, where the spectral index reached a stable value, is chosen to be the inner radius of the annular region. This annular region from $6'$ to $15'$, is used as the source region throughout the rest of the work.

Fig. A2 shows a plot of the Encircled Energy Fraction

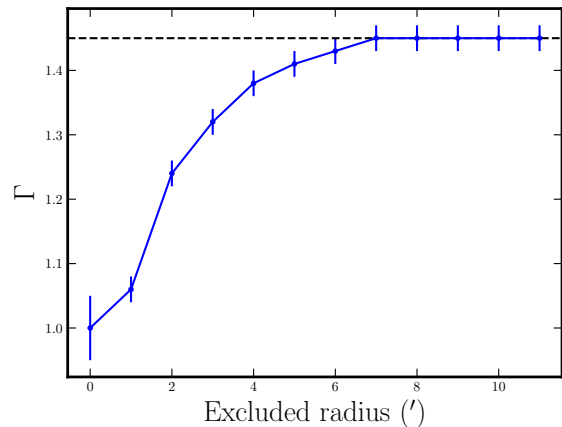


Figure A1. Plot to check the effect of pile-up, following Romano et al. (2006). We use different annular regions in the CCD image, with outer radius fixed at $15'$ from the centroid of the PSF and inner radius progressively excluded. Each spectrum is then fitted with a simple model described in Appendix A. The data points show the spectral index (Γ) as a function of the radius of the inner excluded region. We can observe that the spectral index increases and reaches a stable value roughly the same as the M1/M2 fit parameters. We have, therefore, chosen $6'$ as the inner radius of the selected source region for the spectral study in section 3.2.2.

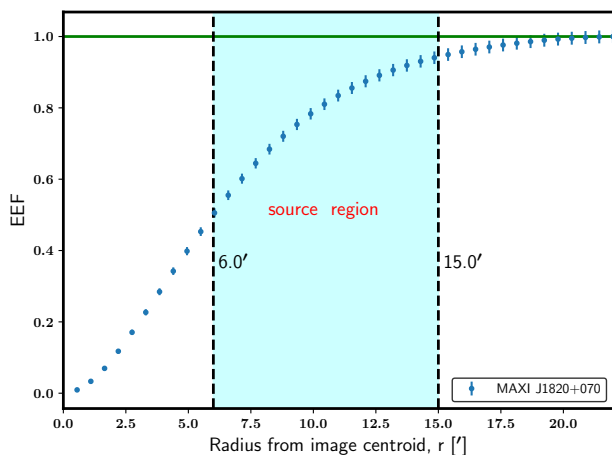


Figure A2. Encircled Energy Fraction (EEF) of the SXT data of MAXI J1820+070, as a function of distance from the centroid of the PSF. The error bars have been multiplied by a factor of 50 for better representation. The shaded region between $6'$ and $15'$ is the chosen source region for our study.

(EEF) for SXT data of MAXI J1820+070. From this plot, we can see that about 44% of photons are encircled within the chosen source region, while a circular region with a radius of $15'$ from the centroid of the PSF should contain about 94% of the photons. Thus, the SXT flux is underestimated by a factor of ~ 2 . This explains the large difference of normalisation factor between the SXT and the other two instruments.

This paper has been typeset from a $\text{T}_{\text{E}}\text{X}/\text{L}^{\text{A}}\text{T}_{\text{E}}\text{X}$ file prepared by the author.